

# Directionally Compliant Legs Enabling Crevasse Traversal in Small Ground-Based Robots

Emily Lathrop, Michael T. Tolley, and Nick Gravish\*

Small ground-based robots show promise for locomotion on complex surfaces. A critical application area for such robots is movement over complex terrain and within constricted space such as narrow gaps in rubble. To contend with this terrain complexity, robots typically require high degree-of-freedom (DOF) limbs. However, for small robot platforms, this approach of high DOF legs is impractical due to actuator limitations. This presents an opportunity to design robots whose morphology enables the outsourcing of computational tasks to the robot body through the use of compliant elements (morphological computation). Herein, a novel robot appendage is developed that can passively compress in a programmed direction in response to environmental constrictions. A robot equipped with these appendages can enter narrow spaces down to 72% of the robot's sprawled body width as well as low ceilings down to 68% its freestanding height. The robot is able to step onto and over small terrain features (1.6× hip height) and navigate various natural terrain types with ease. The results show that these compressible appendages enable versatile robot locomotion for robot exploration in previously unmapped environments.

## 1. Introduction

To successfully deploy in natural environments, mobile robots need to traverse both open and confined spaces as well as transition between terrain types. In recent years, mobile robots have become increasingly capable of navigating in and around open natural spaces such as grassy fields, forest underbrush, and steep hills.<sup>[1–6]</sup> In confined spaces, novel robot designs such as snake-like bodies,<sup>[7,8]</sup> limbs with compliant elements,<sup>[9]</sup> or robots that use limb–wall interactions to their advantage<sup>[10]</sup> have been used to navigate tunnel environments and complete tasks such as pipe inspection or tunnel traversal.<sup>[11]</sup> But so far, less focus has been given to designing versatile robots that can seamlessly transition

between various types of natural environments without the addition of many degrees of freedom (DOF).

When examining classes of mobile robots and the spaces they are designed to move through, we observe that most current mobile robots are designed with a particular environment in mind. Their morphology is then optimized around moving through that environment. As a result, they do not perform well when placed in other environments. For example, wheeled robots perform best on smooth, low-roughness surfaces and cannot traverse large ground obstacles.<sup>[12]</sup> Insect-scale compliant robots can navigate small spaces and tunnels but cannot move over human-scale terrain or obstacles much larger than their body size.<sup>[13]</sup> Robots with rigid limbs use feedback control to walk and run over unstructured natural terrain but cannot compress to enter small spaces.

To create the next generation of versatile exploratory robots that can enter and move about in previously unmapped spaces, new robot designs will need to be able to adapt to environments that can change as they move through them. This can include transitioning between unstructured terrain and confined spaces, moving quickly through many types of natural environments, and negotiating confined spaces where the geometry of the space changes spatially, such as caves and tunnels.

Our work was inspired by biological examples of animals that can move robustly through a wide variety of spaces, such as ants and cockroaches. One strategy that insects often use to navigate obstacles and fit into small spaces is to modify their effective width and height. This phenomenon is seen in ants as they tuck their legs under them to climb through narrow passages.<sup>[14]</sup> It is also seen in sandfish lizards, which reduce their effective width by tucking their legs into their sizes when moving through sand.<sup>[15]</sup> Many animals in nature also use body compliance to squeeze through constrictions. Common examples include octopuses squeezing through small holes<sup>[16]</sup> and cockroaches squeezing under doors.<sup>[10]</sup> In robotic contexts, previous work has shown that embedding compliance into robot bodies can increase stability in cluttered environments.<sup>[1,17]</sup> Other work has shown that body compliance can enable locomotion in confined spaces.<sup>[10,18]</sup> All of the above examples make use of morphological computation, which involves “outsourcing part of control, sensing and computation tasks to the robot body to be handled through emergence of functional behaviours due to properties

E. Lathrop, M. T. Tolley, N. Gravish  
Department of Mechanical and Aerospace Engineering  
University of California San Diego  
La Jolla, CA 92093, USA  
E-mail: ngravish@eng.ucsd.edu

 The ORCID identification number(s) for the author(s) of this article can be found under <https://doi.org/10.1002/aisy.202200258>.

© 2022 The Authors. Advanced Intelligent Systems published by Wiley-VCH GmbH. This is an open access article under the terms of the Creative Commons Attribution License, which permits use, distribution and reproduction in any medium, provided the original work is properly cited.

DOI: 10.1002/aisy.202200258

such as architected kinematics, compliance, natural resonance, damping and friction”.[19] In this way, control and actuation complexity can be reduced through body design.

Our robot appendages were inspired by previous work on ant locomotion in tunnels, where it was found that in unconfined environments, ants use a wide, sprawled posture, but when compressed in tunnels, they narrow their sprawl and shorten their effective leg length by drawing their legs under their bodies.[14] We implemented these design principles in a robot system using telescoping appendages, which achieved the same sprawl and leg length modifications that we see in ants, but through different mechanisms.

We demonstrate that our compliant appendages allow a robot to passively squeeze into small tunnels and under low ceilings and enable locomotion in confined spaces without sacrificing fast and stable locomotion in natural environments. In this work, we present the design of a telescoping leg robot that enables versatile movement in confined spaces (Figure 1a). Our robot can passively compress in response to environmental constrictions and shrink its effective body width and height through the use of collapsing leg segments (Figure 1b). We demonstrate that these appendages allow a robot to passively squeeze into small tunnels and under low ceilings and enable locomotion in confined spaces without sacrificing fast and stable locomotion in natural environments.

## 2. Background

Current metrics of success for mobile robots deployed in the wild are often evaluated through demonstrations across various types of natural terrain, as well as ability to traverse large obstacles, often quantified as maximum step height a robot can traverse

as a function of hip height.[13] In a similar vein, in Figure 2, we seek to quantify existing robots on performance in confined spaces, defined as the ability to modify body cross section to fit into constrictions of varying dimensions. Figure 2a demonstrates the maximum possible height and width compression that current mobile robots are able to achieve relative to the robot’s freestanding dimensions. For example, a 30% width compression means that the robot can decrease its body width by 30%, resulting in a body width that is 70% of the freestanding body width.

### 2.1. Robots in Confined Spaces

Current robots employ several methods to navigate confined spaces that are smaller than their geometry would normally allow. One solution available to robots with a large number of DOF is to reposition joints and limbs to enact maneuvers such as crouching or drawing limbs in from sprawled to more compressed postures.[3,5,20–24] However modifying body cross section in this manner can be slow and computationally intensive. Other mobile robots circumvent this by taking advantage of body compliance[1,10,25,26] to passively squeeze into small spaces. Some examples include flexible shells to squeeze under low ceilings[10] and flexible legs to squeeze through small gaps.[27] This type of strategy falls in the general category of morphological computation, where the mechanism for body shape change in response to environmental conditions is embedded into the body of the robot.[19] This approach can allow robots to use simple, open-loop strategies to passively adjust to variable terrain features without the need for complex sensing or control.[17]

In Figure 2a, we show the maximum body compression along the largest body dimension for many popular mobile-legged

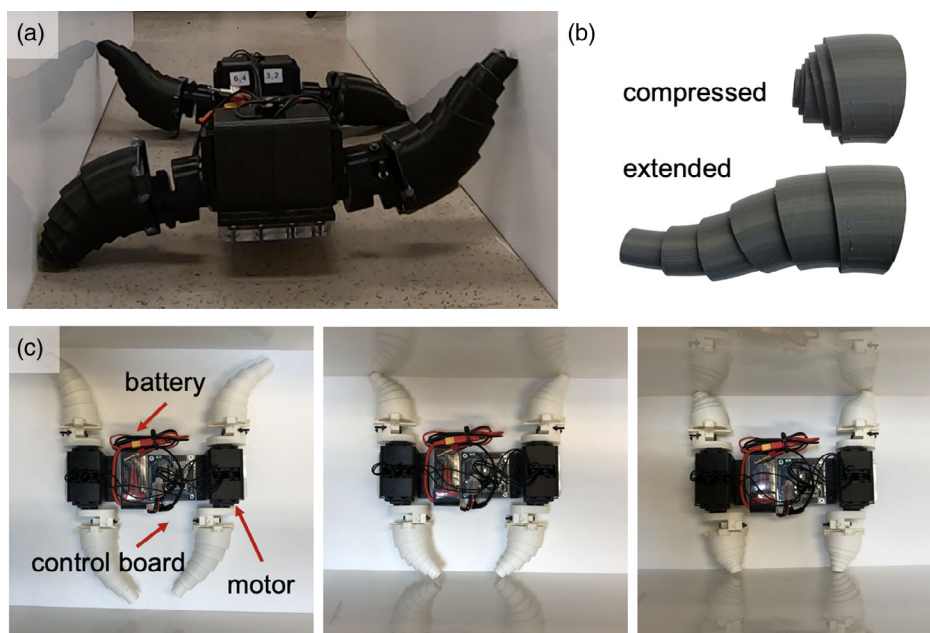


**Figure 1.** Robot with passively telescoping legs. a) Robot walking between two flat walls. b) Internal structure of a single leg consisting of 3D-printed leg segments with internal springs. c) Robot system consisting of an on board battery, control board, and four continuously rotating motors. Robot with telescoping legs fully extended, partially compressed, and fully compressed in a channel.

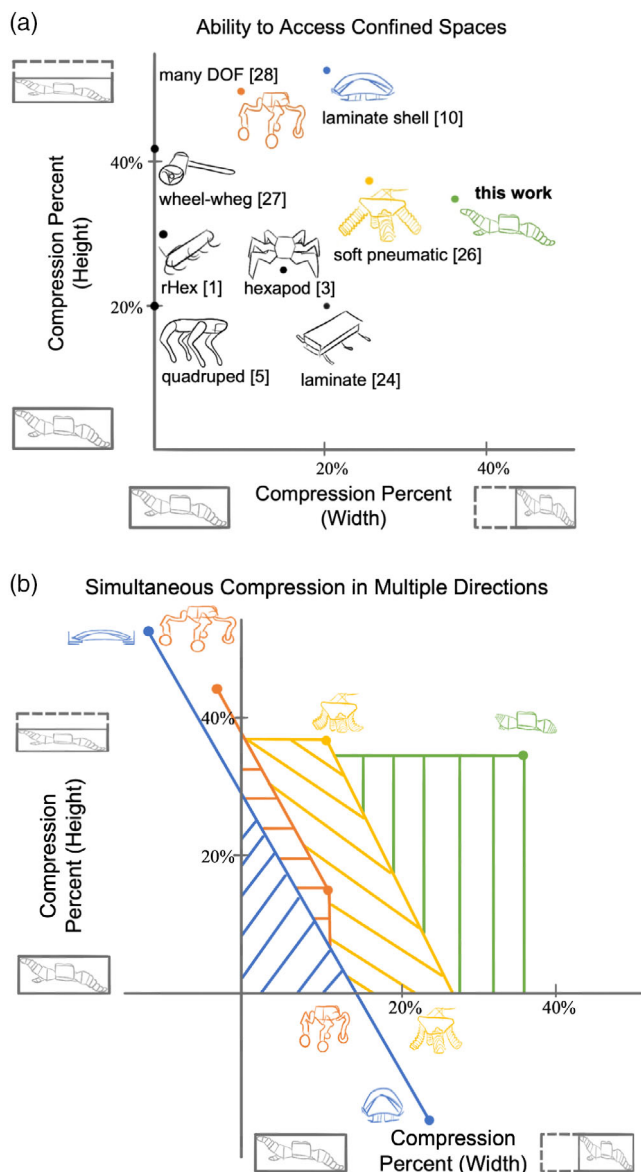


**Figure 2.** Current landscape of legged robot locomotion in confined spaces (See Table S1, Supporting Information, for details). a) Classes of mobile robots graphed on ability to modify body width and height to enter a confined space. Axes display maximum possible body height or width compression as a percentage of freestanding robot height and width, where larger means able to compress more in that dimension. b) Achievable geometries for four classes of robots. Positive values correspond to body compression and negative values correspond to body expansion. Points in the shaded regions represent achievable robot geometries, as well as tunnel cross sections that each robot can produce a valid geometry to traverse.

robots<sup>[1,10,21,24,25,27–29]</sup> (see Table S1, Supporting Information, for details). Although points in this plot capture the limits of possible shape change, it lacks nuance as to actual achievable robot geometries by making the assumption that a robot body is a compressible volume and height, and width compression can be achieved independently. Functionally, this is often not the case.

To further estimate how legged robots can adapt to different confined volumes, we make a constant volume assumption for their body reconfiguration capability. We assume that as body height decreases, to accommodate lower height confines the width must increase accordingly. In Figure 2b, we show results from this analysis for four representative robot platforms. We observe that in all cases, there is a tradeoff between accommodating height and width confinement due to the constant volume nature of many-legged robots (Figure 2b blue, red and yellow curves).

When plotting robot compression, positive values correspond to decreasing a dimension of a robot body and negative values correspond to expanding a dimension of a robot body. Points in the shaded regions correspond to robot geometries, as well as the cross-sectional dimensions of tunnels that each robot can traverse with an appropriate change in geometry. Using this method, one can evaluate the range of confined spaces that a robot can access and move within. These observations demonstrate the need for compressible volume robots and robot appendages that can compress in 1D without expanding in another.

### 3. Design

#### 3.1. Leg Geometry

Our robot appendages featured a telescoping design inspired from work done on concentric tube actuators.<sup>[30–32]</sup> This design enabled leg compression without expansion in another dimension by allowing the leg to collapse into itself. Our appendages differed in form and function from other concentric tube designs<sup>[33,34]</sup> by the addition of internal springs between each leg segment. This allowed the appendages to support the robot body weight with minimal spring (and thus leg) compression. To maximize freestanding body height, we attached the appendages to the robot body in an orientation such that the internal springs were primarily pointed in the horizontal direction, minimizing spring compression in the vertical direction that would occur due to the robot's body weight. We hypothesized that there existed an optimal leg spring stiffness that was low enough to allow passive compression when interacting with narrow walls but also high enough to support the weight of the robot without collapsing inwards.

The leg surface geometry was created in unity using an open-source design tool.<sup>[32]</sup> Using this tool, we created a six-segment nested telescoping structure that followed the path of a cubic Bézier curve (Figure 3b). Each segment consisted of a hollow cylinder of decreasing radius with two guiding grooves running along the inside of each cylinder to inhibit rotation between segments. We adjusted parameters such as leg curvature, leg segment taper rate, wall thickness, and gap width between leg segments to fabricate legs that would telescope smoothly into each other with minimal friction between segments.

Each segment was held into the leg assembly by a lip at the proximal end of the cylinder. A flat plate was press fit into the end of each cylinder and a spring attached to each flat plate. Each spring faced internally into the body of the cylinder (Figure 3a). These springs spanned from flat plate to flat plate and were compressed when the legs telescoped in to each other.

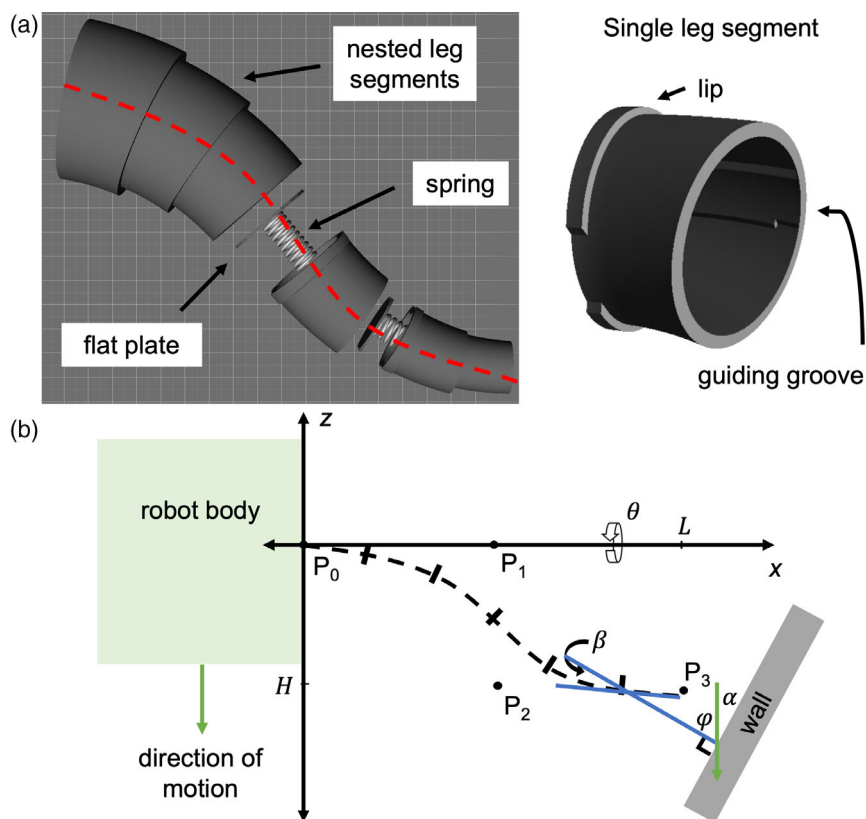


**Figure 3.** Leg design and model. a) Internal structure of a single leg consisting of 3D-printed leg segments with internal springs attached to plates located at the end of each leg segment. Leg is assembled sequentially. b) Top-down view of a leg interacting with an angled wall where  $P_0$  through  $P_3$  are control points for the Bézier spline that defines the leg,  $\theta$  is the angle by which the leg rotates around the hip joint,  $L$  is the width of the leg,  $H$  is the height of the leg (hip height),  $\alpha$  is the angle of a wall with respect to the robot direction of motion,  $\phi = 90 - \alpha$  is the wall normal, and  $\beta$  is the angle between the leg spline tangent and phi.

### 3.2. Leg Fabrication

The segments and end caps were printed individually out of acrylonitrile butadiene styrene (ABS) on a commercially available 3D printer (Prusa Research). During the printing process, we tailored various parameters for the specific printer model and filament material, so that the segments would nest tightly to reduce deflection in directions other than along the length of the spline. Printing parameters were also tuned to minimize friction between pieces to allow the leg segments to telescope smoothly into each other. These parameters included taper angle of each segment, gap width between consecutive segments, and the size and shape of the internal guiding grooves (Table S2, Supporting Information).

Once printed, the spring caps were assembled by gluing one end of each of the five springs to one face of each of the five largest end caps. An exploded view of the leg components can be seen in Figure 3a. The leg was then assembled, sequentially starting from the smallest segment by press-fitting a spring cap into the distal end of the segment followed by inserting the segment into its next larger neighbor and repeating the process until all segments are assembled. The fully assembled leg can be seen attached to a robot in Figure 1a.

### 3.3. Robot Platform

Our robot platform consisted of four telescoping appendages mounted to four high-torque servo motors (dynamixel series). The robot was controlled via an Arbotix-M board and powered by an on-board lithium polymer (Li-Po) battery. The motors, control board, and battery were mounted to a flat plate of laser-cut acrylic, which served as the robot backbone. The robot used a continuous angular rotation diagonal coupled gait. The full dimensions of the robot platform were 31 cm in width, 20 cm in length, and 7.75 cm in height. The dimensions of a single leg were 8.8 cm in width and 5.5 cm in height. The weight of a single leg was 29.2 g and the weight of the assembled robot system was 830 g.

## 4. Modeling and Simulation

### 4.1. Leg Model

To predict the passive compression abilities of an appendage, we created a model of the motion of a single leg interacting with obstacles. The goal of the model was to determine how changing

leg shape affected the passive compression ability of the legs. We first modeled a single leg interacting with a sidewall in order to predict the passive compression behavior of the robot walking through a narrow channel.

The fully extended leg is modeled and defined by a cubic Bézier spline with control points  $P_0$  through  $P_3$ . To create the leg segments, the spline was subdivided into six segments. The spline was defined as

$$\tilde{B}(t) = (1-t)^3 P_0 + 3(1-t)^2 t P_1 + 3(1-t)t^2 P_2 + t^3 P_3, t \in [0, 1] \quad (1)$$

In each gait cycle, the motor rotated the leg by  $\theta$  around the motor axis  $x$  to give leg position

$$\tilde{B}(\theta, t) = R_x(\theta) \tilde{B}(t) \quad (2)$$

where  $P_0 \rightarrow P_3 \in \mathbb{R}^3$  were spline control points originating in the  $xz$  plane with  $P_0 = [0, 0, 0]$  in the base of the leg frame (Figure 3b).

As a leg encountered a flat wall obstacle positioned at angle  $\phi$  with respect to the robot direction of motion (Figure 3b), a side-wall normal can be written as  $N(x, y, z) = (\sin \phi, 0, \cos \phi)$  and a ground normal can be written as  $N = (0, 1, 0)$ . The angle  $\beta$  between the tangent to the leg spline and the normal to the wall was used to determine the component of force causing spring compression in the leg.

$$\cos \beta(\theta, t) = \frac{|B'(\theta, t) \cdot N|}{|B'(\theta, t)| |N|} \quad (3)$$

When the robot moved forward in a channel, the force compressing the internal springs is the component of the traction force pointed in the direction of the leg spline. This force is written as

$F_c(\theta) = T \cos \phi \cos \beta$ , where  $T = mg \tan(\mu)$  is the traction force generated by the robot while walking,  $\mu$  is the friction coefficient between the robot leg and the ground, and  $m$  is the mass of the robot. The forces opposing leg compression were the sliding friction between the segments  $F_f(\theta) = T \cos \phi \sin \beta$  and the spring's restoring force.

We used this model to calculate the leg length change of each segment caused by the compression force described above as a leg interacted with a wall of angle  $\phi$ . During a cycle, passive leg compression was maximized when  $\theta = \frac{3\pi}{2}$  which corresponded to when the leg was pointed forward (in the  $xz$  plane).

## 4.2. Walking Robot Simulation

To determine the optimal spring stiffness for the springs inside the telescoping legs, we simulated the robot traversing two high walls of varying width and swept through a range of spring stiffness values, observing the resulting speed of the robot through the channel (Figure 6a). The variance between trials can be accounted for by varying the initial phase of the robot legs between simulation runs. We used a simulation environment tailored to robotic systems (CoppeliaSim) running a popular rigid body dynamics solver (Bullet 2.78). The spring-mediated telescoping action was simulated by attaching virtual prismatic

joints in the spring-damper mode between the leg segments. In the simulation, we set the sliding friction between leg segments to zero in order to more closely examine the dynamic robot behavior and the interactions the robot legs had with their environment, eliminating the within-leg interactions seen in the analytical model above.

## 5. Results

### 5.1. Model Fitting

After developing a leg compression model that accounted for internal friction, we investigated how modifying parameters such as leg stiffness and leg shape could minimize the force needed to compress the legs across a range of channel angles. We first measured the force–displacement compression curves of 3D-printed appendages using a motorized test stand (Mark-10 ESM750S, Figure 4a). We then used these curves to estimate a lumped parameter value for the friction coefficient  $\mu_s$  between leg segments ( $\mu_s = .75$ ). This parameter accounted for fabrication-induced friction such as layer roughness and print direction.

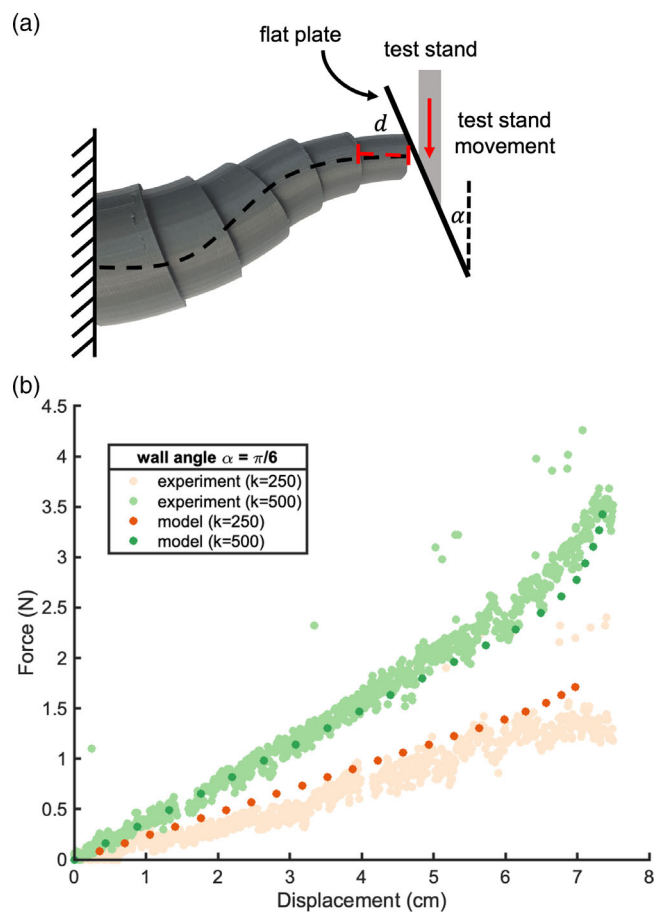


**Figure 4.** Force versus displacement test on a single leg. a) Force–displacement test setup. b) Force displacement tests were performed on telescoping legs of two stiffnesses in order to determine a lumped parameter value for the model that describes the friction between leg segments within a leg.

Using this value, our model matched experimental curves for both a very stiff leg ( $k=500$ ) and an optimal stiffness leg ( $k=250$ ), interacting with a representative wall of angle  $\alpha = \pi/6$  from parallel (Figure 4b).

### 5.2. Optimal Leg Shape

After matching our model to experimental curves, we investigated the effect of spline shape on the passive compressive ability of the telescoping legs while the robot is inside a channel. We examined how the maximum leg compression varied as the spline shape changed with the goal of choosing a leg shape that would offer high passive compression when it encountered walls of a wide range of orientations with respect to the leg.

We found that the passive leg compression in both the horizontal and vertical directions was dependent on the shape of the spline and that the optimal shape consisted of a spline with control points  $P_0 = (0, 0)$ ,

$P_1 = (L/2 - 1.46, 0)$ ,  $P_2 = (L/2 + 1.46, H)$ , and  $P_3 = (L, H)$  (see Figure 5a,b). A spline with these control points achieved a passive width compression of on average 82.4% of the compressible length of the leg (Figure 5a) and a height compression of 79% (Figure 5b) when walking through channels with contact wall angles ranging from 0 (parallel) to  $\pi/4$  radians. We found that leg compressibility varies depending on the angle of the channel walls (Figure 5c,d).

### 5.3. Optimal Leg Stiffness

We next used simulation to determine the optimal stiffness for the springs embedded in the legs. We simulated how varying the stiffness of the springs between leg segments affected the walking speed of the robot inside a channel. Intuitively, we expected the optimal spring stiffness to be a balance of a high-enough stiffness to support the weight of the robot, but also a low-enough stiffness so that the legs would compress when confined in a channel.

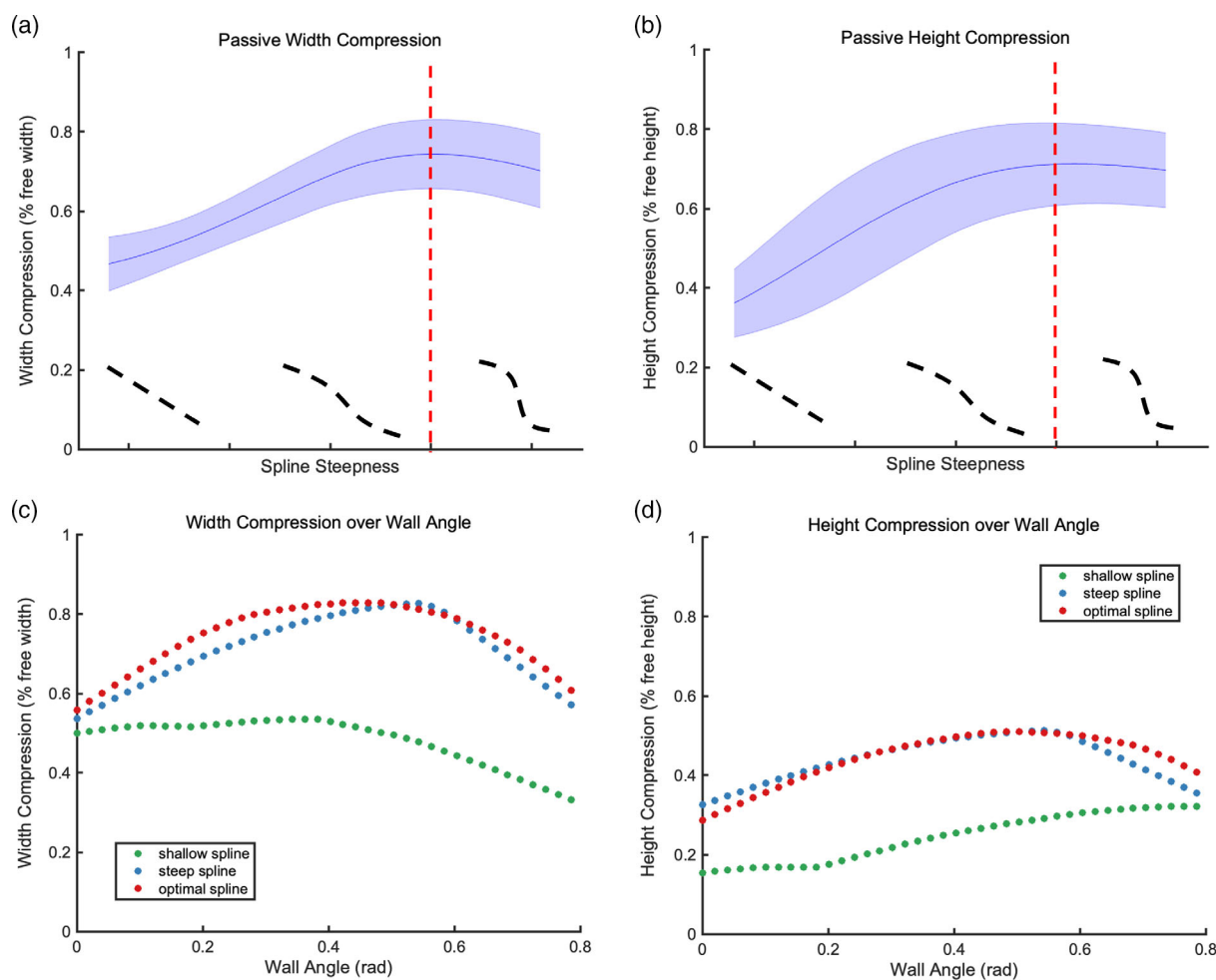


**Figure 5.** Maximum achievable passive leg compression when interacting with walls over a range of spline shapes. a) Maximum leg compression in the horizontal direction that can be achieved passively by the force of the robot leg hitting a wall as spline shape varies. Representative spline shapes are shown along the axis. Line and shaded region correspond to the average and standard deviation for maximum leg compression over walls ranging from 0 to  $\pi/4$  rad. b) Maximum leg compression in the vertical direction that can be achieved passively, averaged over a range of wall angles. c) Passive width compression varies depending on the angle of the wall the limb is interacting with and the shape of the spline. d) Passive height compression varies similarly.

In the simulation, the robot began in open flat ground and then was funneled into a narrow channel. Channel widths were varied from 100% robot body width (legs were completely uncompressed while walking in the channel) to 70% robot body width (legs were compressed 30% while walking in the channel). We then measured the time to traverse the channel to obtain robot walking speed in the channel (Figure 6b). We varied the starting phase of the legs between trials, which is reflected in the error bars in Figure 6b.

Our simulation results showed that the optimal spring stiffness for maximizing robot speed in a channel was dependent on the width of the channel (Figure 6b). We averaged performance over a range of moderately narrow channels (70–90% of the unconstrained robot width) and chose a spring stiffness of  $k = 250$  to implement on our robot platform.

#### 5.4. Leg Stiffness Validation on Robot Platform

We attached legs of various stiffnesses to our experimental platform and showed that the optimal stiffness legs performed best in a wide range of scenarios. We fabricated three robot platforms: one featuring telescoping legs with no springs, one with internal springs of the optimal spring stiffness found in simulation ( $k = 250$ ), and one featuring stiff springs ( $k = 500$ ). We compared

walking performance of these three robots through a channel formed from two vertical acrylic plates and found that, over a wide range of narrow channels, the robot with the optimal spring stiffness was able to walk faster than the robot with stiff internal springs (Figure 7a), with exception of unconfined walking, where the speed was similar. The large speed decrease in the stiff legs can be explained by the intuition that if one forces a leg with very stiff springs to compress a large amount, the restoring force results in the legs jamming themselves between the walls, hindering progress.

The robot equipped with legs with no internal springs resulted in each leg fully collapsing into itself, resulting in what was functionally a wheel composed of the largest leg segment. The length of these legs was not variable, and their speed was constant and dependent on wheel radius. Although these wheel legs resulted in a narrower overall body width, they were not able to achieve the same maximum speeds as their legged counterparts in less confined spaces (Figure 7a). Additionally, these wheel legs were unable to navigate tall steps or natural terrain with large features.

#### 5.5. Speed Dependence on Leg Length

Robot walking speed is a function of stride length and stride frequency. On this robot platform, stride length was directly

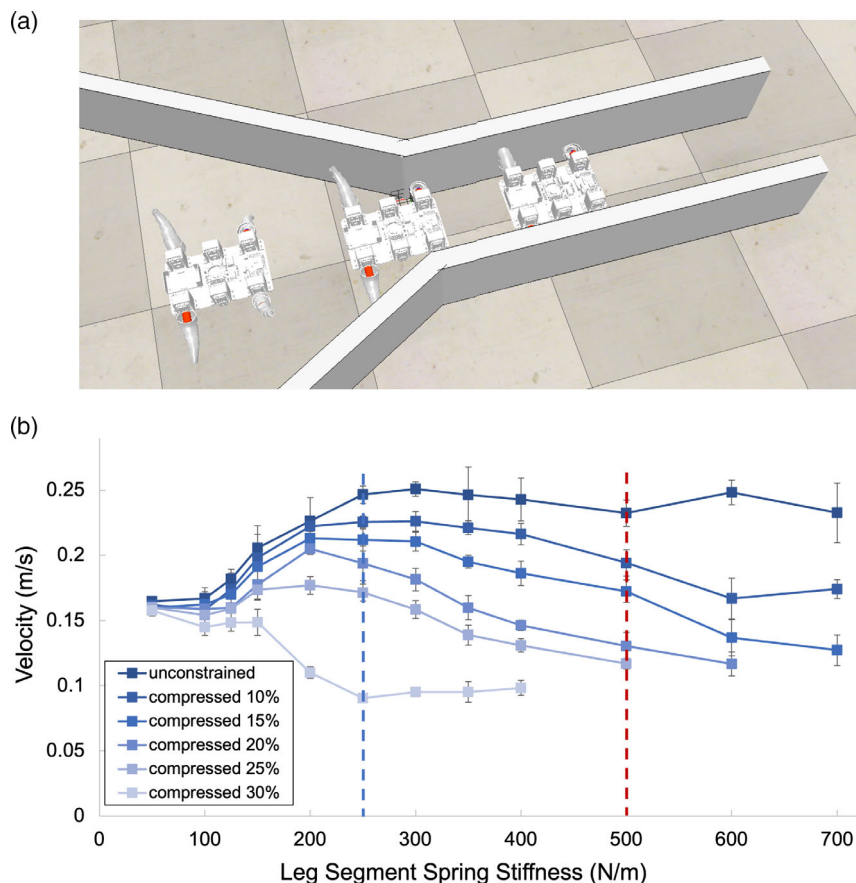


**Figure 6.** Simulation to determine optimal spring stiffness. a) Simulation setup in CoppeliaSim. b) Robot walking speed in channels of various widths and with legs of varying stiffness. Starting phase of legs was varied between trials ( $n = 5$ ). Dotted lines depict the stiffness values for the two legs tested experimentally: blue for the optimal stiffness case and red for the too stiff case.

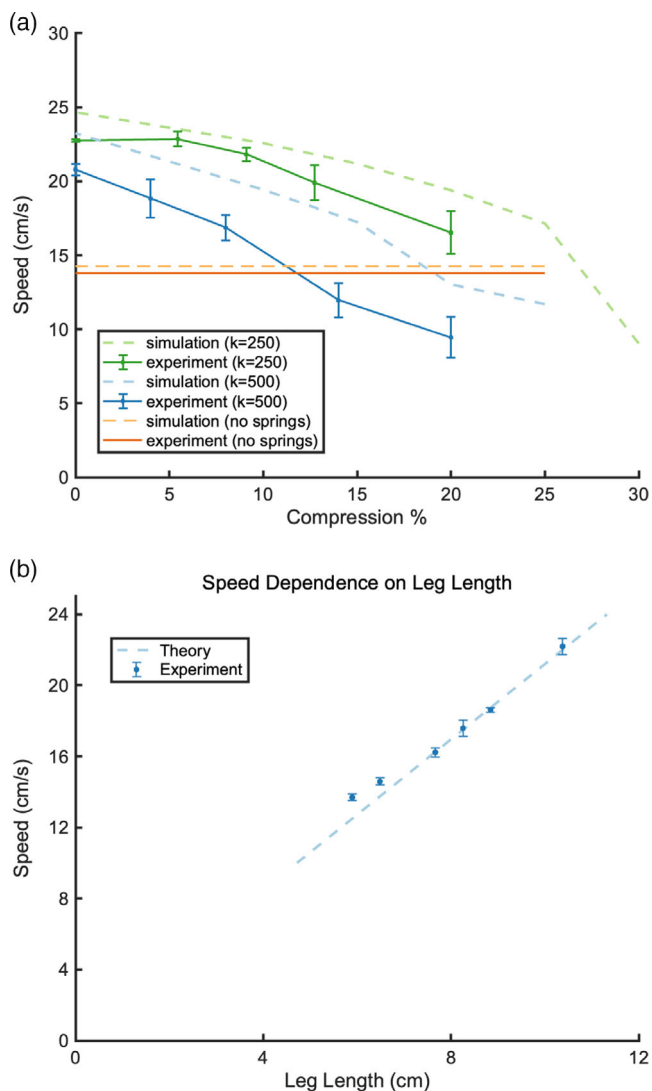


**Figure 7.** Robot walking speed in narrow channels. a) Speed versus channel width for a robot equipped with spring legs of optimal and nonoptimal stiffnesses, as well as with telescoping legs with no internal springs, which fully collapse into the largest segment, creating a consistent, wheel-like rolling motion with the largest segment serving as a wheel. b) Speed over flat ground is dependent on leg length. Legs were constrained to a fixed length and speed was measured in flat, open terrain ( $N = 3$ ).

proportional to the hip height of the robot, which was a function of leg length (Figure 7b). We experimentally validated the dependence of speed on leg length by fixing the legs in partially compressed positions and measuring walking speed over flat ground ( $N = 3$ ). This relationship motivated the need for long but compressible appendages to maximize speed in open terrain yet still allow confined spaces to be accessible. The speed drop-off seen in confined spaces (Figure 7a) was also explained by this relationship: narrow channels caused greater leg compression, which resulted in a speed that was proportional to that compressed leg length.

## 5.6. Robot Demonstrations

In the following section, we demonstrate that our robot is successful at navigating many diverse natural environments including confined spaces, steps, and rough ground. All trials were conducted with the robot platform and walking gait described in Section 3.3, with  $N = 3$ .

### 5.6.1. Entering and Traversing Narrow Channels

Our robot was capable of transitioning from free walking to entering an angled and narrowing tunnel narrower than the robot's body width (Figure 8a) and walked in both parallel and angled channels. Channel widths tested ranged from 25 to 35 cm in width and speed was measured over a channel length of 90 cm. The uncompressed robot width was 30.5 cm. At channel widths larger than 80%, the robot was able to enter and walk inside with a success rate of 100%. The minimum channel width the robot was able to enter and walk through was 72% of the robot's uncompressed width, with a success rate of 50%. This was close to the theoretical limit of 65% of the robot's uncompressed width, which was determined by the total width of the rigid components of the robot body.

In both simulation and experiment, we demonstrated that robot speed decreased as gap width increased. We also demonstrated that the robot with optimal leg stiffness moved through confined spaces faster than the robot featuring stiffer legs (Figure 7a). Although there were statistically significant differences between simulation and experiment, we saw good shape agreement for both stiffness tested. In the  $k = 250$  case, as the channel narrowed, both simulation and experiment showed a slow performance decrease followed by a more rapid performance decrease. In the  $k = 500$  case the simulation and experiment had similar slopes with some magnitude discrepancies. We hypothesize that the differences in magnitude may be due to the simulation not appropriately capturing the effects of sliding friction between leg segments.

### 5.6.2. Squeezing under Low Roofs

The robot legs were able to passively compress to squeeze the robot under a low roof that is 68% of freestanding body height (Figure 8b) with an 100% success rate. This compression was in part driven by leg compression and in part driven by the pitch and roll motion of the alternating quadruped gait, which increased the amount the leg segments are pointed toward the ceiling during portions of the leg cycle, bringing  $\beta$  closer to parallel with the wall normal. Freestanding robot height was 11 cm and the maximum height a leg achieved during each cycle due to the unstable gait was 14 cm.

### 5.6.3. Step Traversal

These appendages also performed well at tasks such as step traversal. Our robot reliably climbed onto and over obstacles  $1.6\times$  its hip height ( $N = 5$  with an 100% success rate), which is consistent with existing legged robot traversal abilities.<sup>[13]</sup>

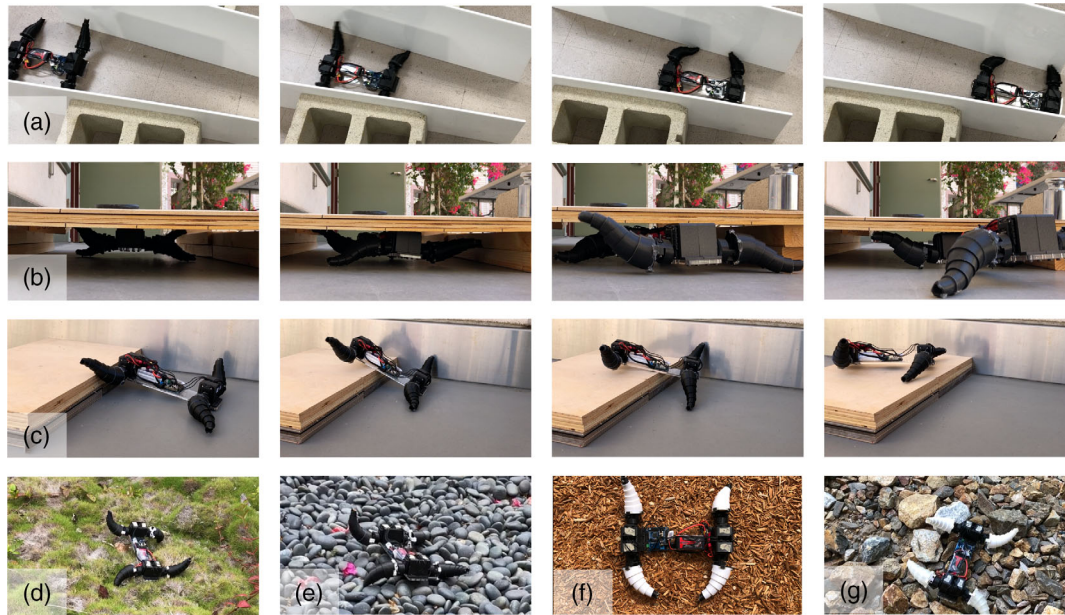


**Figure 8.** Robot in the wild. a) Demonstration of robot walking between narrowing walls whose minimum width is 72% freestanding body width. b) Demonstration of robot walking under a low ceiling 68% of freestanding height. c) Robot climbing over a step ( $1.6\times$  hip height). d–g) Robot walking over unstructured terrain (tufted grass, river rock, mulch, variable size crushed granite).

#### 5.6.4. Natural Terrain Locomotion

Our robot was also able to walk successfully over several types of unstructured terrain. We demonstrated successful locomotion over tufted grass (average length = 3 cm, average diameter of tufts = 20 cm, dry conditions), loose river rock (average diameter = 5 cm, depth = 15 cm, smooth surface finish, loosely packed, dry conditions), mulch (average length = 2 cm, depth = 10 cm, loosely packed, dry conditions), and a sharp rock field (rock diameters ranging from 1–15 cm, depth = 5–10 cm, rough surface finish, loosely packed, dry conditions).

Over a distance over 1.2 m, the robot traversed tufted grass (Figure 8d) with an average speed of  $16.1\text{ cm s}^{-1}$  ( $\sigma = .3\text{ cm s}^{-1}$ ,  $N = 3$ ), river rock (Figure 8e) with an average speed of  $18.7\text{ cm s}^{-1}$  ( $N = 3$ ), loose mulch (Figure 8f) with an average speed of  $16.1\text{ cm s}^{-1}$  ( $\sigma = 1.03\text{ cm s}^{-1}$ ,  $N = 3$ ), and jagged rock (Figure 8g) with an average speed of  $14.8\text{ cm s}^{-1}$  ( $\sigma = .97\text{ cm s}^{-1}$ ,  $N = 3$ ). Over terrain with uniform features (tufted grass, river rock, loose mulch), the robot was able to maintain a constant speed, but over nonuniform terrain such as the sharp rock field, the robot occasionally lost traction and would spin in place for up to one leg cycle before regaining traction and resuming forward progress.

In summary, the intrinsic compliance of the telescoping structures created dynamic stability over many types of unstructured terrain. The main limiting factor was in the size of obstacles: the robot was not able to reliably climb over obstacles protruding more than about 8 cm from the surrounding obstacles, which was consistent with the  $1.6\times$  hip height limitation found in the step traversal tests.

## 6. Conclusion

In this work, we have presented the design of a telescoping appendage that allowed a robot to modify its leg length in response to environmental constrictions without added actuation or power requirements. We optimized the shape and stiffness of these telescoping appendages and demonstrated that a robot equipped with these appendages can passively enter narrow channels and move quickly through them. We have also demonstrated that a robot equipped with these appendages successfully navigated natural terrain obstacles such as rough ground and tall steps.

In the future, active stiffness modulation between leg segments could allow stiffness tuning in response to terrain type: for example, high stiffness while walking over flat ground and lower stiffness when moving through confined spaces. Active control of stiffness for enhancing legged locomotion has been studied in other works.<sup>[9,35,36]</sup> Additionally, low-power adjustable stiffness mechanisms<sup>[37–39]</sup> offer the possibility of incorporating tunable stiffness without drastically increasing power requirements.

The appendages presented in this work offer exciting opportunities for translation to smaller scales where manufacturing, powering, and actuating many DOFs become difficult. Creating versatility through morphology can reduce actuated DOFs and reduce power needs. At small scales ( $10^{-3}$ – $10^{-1}$  m features), the ability to navigate body-sized obstacles becomes increasingly important, since this scale of terrain presents much more height variation and constriction, relative to body size, than large-scale terrain ( $10^1$  m features).<sup>[40,41]</sup> At the lower limit of

miniaturization, the prismatic system presented in this work becomes difficult to fabricate, and frictional effects between leg segments greatly limit the performance of sliding components. Future miniaturized designs could replace sliding components with flexure-based collapsing designs.

In this work, we developed a collapsible leg that enables navigation of complex terrain using minimal control feedback. This passive alternative to high-DOF limbs can enable the design of smaller robots without sacrificing terrain adaptability or versatile movement. The ability for a robot to modify body size is useful when looking to deploy robots in environments with unknown features and obstacles such as cave systems or building rubble. In these situations, it is often not possible to predetermine the types of obstacles a robot may encounter and it is advantageous to have a robot that can respond to constrictions of varying geometries. In the future, designs that use morphological computation to reduce actuation requirements can enable small and versatile robots for applications such as search and rescue, disaster response, mapping of small interior spaces, and exploration in caves and tunnels.

## Supporting Information

Supporting Information is available from the Wiley Online Library or from the author.

## Acknowledgements

This work was supported by the US National Science Foundation CAREER grant #2048235 (IOS). The work of E.L. was supported by the National Science Foundation Graduate Research Fellowship under grant no. DGE-1650112. This work was supported by the Office of Naval Research (Grant No. N00014-20-1-2373). The authors thank Saurabh Jadhav for insightful feedback.

## Conflict of Interest

The authors declare no conflict of interest.

## Data Availability Statement

The data that support the findings of this study are available from the corresponding author upon reasonable request.

## Keywords

mobile robots, morphological computations, natural terrain locomotion, robotics

Received: August 11, 2022  
Revised: November 14, 2022  
Published online:

- [1] U. Saranlı, M. Buehler, D. E. Koditschek, *Int. J. Rob. Res.* **2001**, *20*, 616.  
[2] M. Kalakrishnan, J. Buchli, P. Pastor, M. Mistry, S. Schaal, in *2010 IEEE Int. Conf. Robotics and Automation*, IEEE, Piscataway, NJ **2010**, pp. 2665–2670.  
[3] M. Bjelonic, N. Kottege, T. Homberger, P. Borges, P. Beckerle, M. Chli, *J. Field Rob.* **2018**, *35*, 1063.

- [4] J. Faigl, P. Čížek, *Rob. Auton. Syst.* **2019**, *116*, 136.  
[5] A. Bouman, M. F. Ginting, N. Alatur, M. Palieri, D. D. Fan, T. Touma, T. Pailevanian, S.-K. Kim, K. Otsu, J. Burdick, A. A. Agha-Mohammadi, in *2020 IEEE/RSJ Int. Conf. Intelligent Robots and Systems (IROS)*, IEEE, Piscataway, NJ **2020**, pp. 2518–2525.  
[6] J. Lee, J. Hwangbo, L. Wellhausen, V. Koltun, M. Hutter, *Sci. Rob.* **2020**, *5*, eabc5986.  
[7] T. Wang, J. Whitman, M. Travers, H. Choset, in *2020 American Control Conf. (ACC)*, IEEE, Piscataway, NJ **2020**, pp. 2458–2463.  
[8] H. C. Astley, J. M. Rieser, A. Kaba, V. M. Paez, I. Tomkinson, J. R. Mendelson, D. I. Goldman, *Bioinspiration Biomimetics* **2020**, *15*, 065005.  
[9] H. Chang, J. Chang, G. Clifton, N. Gravish, *Bioinspiration Biomimetics* **2021**, *16*, 056001.  
[10] K. Jayaram, R. J. Full, *Proc. Natl. Acad. Sci.* **2016**, *113*, E950.  
[11] N. S. Roslin, A. Anuar, M. F. A. Jalal, K. S. M. Sahari, *Procedia Eng.* **2012**, *41*, 1456.  
[12] L. Bruzzone, G. Quaglia, *Mech. Sci.* **2012**, *3*, 49.  
[13] S. W. Gart, C. Li, *Bioinspiration Biomimetics* **2018**, *13*, 026005.  
[14] N. Gravish, D. Monaenkova, M. A. Goodisman, D. I. Goldman, *Proc. Natl. Acad. Sci.* **2013**, *110*, 9746.  
[15] R. D. Maladen, Y. Ding, C. Li, D. I. Goldman, *Science* **2009**, *325*, 314.  
[16] C. Laschi, M. Cianchetti, B. Mazzolai, L. Margheri, M. Follador, P. Dario, *Adv. Rob.* **2012**, *26*, 709.  
[17] Y. Ozkan-Aydin, D. I. Goldman, *Sci. Rob.* **2021**, *6*, eabf1628.  
[18] Y. Ozkan-Aydin, B. Liu, A. C. Ferrero, M. Seidel, F. L. Hammond, D. I. Goldman, *Bioinspiration Biomimetics* **2021**, *17*, 016001.  
[19] K. Ghazi-Zahedi, J. Rieffel, S. Schmitt, H. Hauser, *Front. Rob. AI* **2021**, *8*, 159.  
[20] P. Hebert, M. Bajracharya, J. Ma, N. Hudson, A. Aydemir, J. Reid, C. Bergh, J. Borders, M. Frost, M. Hagman, J. Leichty, *J. Field Rob.* **2015**, *32*, 255.  
[21] G. Bleidt, M. J. Powell, B. Katz, J. Di Carlo, P. M. Wensing, S. Kim, in *2018 IEEE/RSJ Int. Conf. Intelligent Robots and Systems (IROS)*, IEEE, Piscataway, NJ **2018**, pp. 2245–2252.  
[22] C. Semini, N. G. Tsagarakis, E. Guglielmino, M. Focchi, F. Cannella, D. G. Caldwell, *Proc. Inst. Mech. Eng., Part I: J. Syst. Control Eng.* **2011**, *225*, 831.  
[23] M. Hutter, C. Gehring, D. Jud, A. Lauber, C. D. Bellicoso, V. Tsounis, J. Hwangbo, K. Bodie, P. Fankhauser, M. Bloesch, R. Diethelm, in *2016 IEEE/RSJ Int. Conf. Intelligent Robots and Systems (IROS)*, IEEE, Piscataway, NJ **2016**, pp. 38–44.  
[24] R. Buchanan, T. Bandyopadhyay, M. Bjelonic, L. Wellhausen, M. Hutter, N. Kottege, *IEEE Rob. Autom. Lett.* **2019**, *4*, 2148.  
[25] P. Birkmeyer, K. Peterson, R. S. Fearing, in *2009 IEEE/RSJ Int. Conf. Intelligent Robots and Systems*, IEEE, Piscataway, NJ **2009**, pp. 2683–2689.  
[26] D. W. Haldane, K. C. Peterson, F. L. G. Bermudez, R. S. Fearing, in *2013 IEEE Int. Conf. Robotics and Automation*, IEEE, Piscataway, NJ **2013**, pp. 3279–3286.  
[27] D. Drotman, S. Jadhav, M. Karimi, P. de Zonia, M. T. Tolley, in *2017 IEEE Int. Conf. Robotics and Automation (ICRA)*, IEEE, Piscataway, NJ **2017**, pp. 5532–5538.  
[28] Y.-S. Kim, G.-P. Jung, H. Kim, K.-J. Cho, C.-N. Chu, in *2013 IEEE Int. Conf. Robotics and Automation*, IEEE, Piscataway, NJ **2013**, pp. 5625–5630.  
[29] B. W. Satzinger, C. Lau, M. Byl, K. Byl, in *Experimental Robotics: The 14th Int. Symp. on Experimental Robotics* (Eds. M. A. Hsieh, O. Khatib, V. Kumar), Springer International Publishing, Cham **2016**, pp. 33–46.  
[30] P. E. Dupont, J. Lock, B. Itkowitz, E. Butler, *IEEE Trans. Rob.* **2009**, *26*, 209.  
[31] T. K. Morimoto, A. M. Okamura, *IEEE Trans. Rob.* **2016**, *32*, 1419.  
[32] C. Yu, K. Crane, S. Coros, *ACM Trans. Graphics (TOG)* **2017**, *36*, 1.

- [33] J. Hodgins, in *Proc. 1988 IEEE Int. Conf. Robotics and Automation*, IEEE, Piscataway, NJ **1988**, pp. 824–826.
- [34] A. Nubiola, M. Slamani, I. A. Bonev, *Precis. Eng.* **2013**, *37*, 451.
- [35] A. M. Hoover, S. Burden, X.-Y. Fu, S. S. Sastry, R. S. Fearing, in *2010 3rd IEEE RAS & EMBS Int. Conf. Biomedical Robotics and Biomechatronics*, IEEE, Piscataway, NJ **2010**, pp. 869–876.
- [36] C. Semini, V. Barasuol, T. Boaventura, M. Frigerio, M. Focchi, D. G. Caldwell, J. Buchli, *Int. J. Rob. Res.* **2015**, *34*, 1003.
- [37] K. W. Hollander, T. G. Sugar, D. E. Herring, in *9th Int. Conf. Rehabilitation Robotics, 2005. ICORR 2005*, IEEE, Piscataway, NJ **2005**, pp. 113–118.
- [38] A. G. Rodríguez, J. Chacón, A. Donoso, A. G. Rodríguez, *Mech. Mach. Theory* **2011**, *46*, 1970.
- [39] V. Chalvet, D. J. Braun, *IEEE Trans. Rob.* **2017**, *33*, 1002.
- [40] B. B. Mandelbrot, B. B. Mandelbrot, *The Fractal Geometry of Nature*, Vol. 1, WH Freeman, New York, NY **1982**.
- [41] M. Kaspari, M. Weiser, *Funct. Ecol.* **1999**, *13*, 530.